J Appl Electrochem (2013) 43:705–710
DOI 10.1007/s10800-013-0559-9

ORIGINAL PAPER

Control synthesis and lithium ion battery performance of manganese dioxide nanowires with tunable structures but similar morphology

Yi Zhang · Hao Liu · Zehua Zhu · Ka-Wai Wong · Rui Mi · Jun Mei · Woon-Ming Lau

Received: 25 March 2013 / Accepted: 8 May 2013 / Published online: 15 May 2013

Abstract Manganese dioxides (MnO_2) with controllable crystalline structure were synthesized by varying the synthesis conditions through a hydrothermal route with $KMnO_4$ and $MnSO_4{\cdot}H_2O$ as precursors. Crystalline structures and morphologies of the samples were characterized by X-ray diffraction, scanning electron microscopy, transmission electron microscopy. The paper studied the nanowires growth mechanism under different experimental conditions, and the resulting lithium storage performance of MnO_2 nanowires with different crystalline structure was also discussed.

Keywords Manganese dioxide · Hydrothermal route · Electrochemical performance

1 Introduction

Manganese oxides and related materials have received great attentions in many applications such as molecular/ion sieves [1], catalysts [2] and Li–ion batteries [3], owing to their ideal electrochemical behavior, low cost, and environmental compatibility [4]. Because of its excellent physical and chemical properties under ambient conditions, manganese dioxide (MnO_2) is one of the most attractive inorganic materials [5, 6]. MnO_2 has several kinds of flexible crystallographic structures such as α-, β-, γ-, δ-, and λ-MnO_2, the different structures being made of [MnO_6] octahedron with different connectivities [7]. The α-, β-, and γ-MnO_2 consist of one-dimensional (1D) tunnels with $X*X$ octahedral cross-section ($X = 1$, 2, 3, or 4) in their structure; δ-phase is a two-dimensional-layered compound; and λ-form has a three-dimensional (3D) spinel structure [8]. In this study, we focused on one-dimensional nanostructured materials as they are expected to play an important role in fabricating the next generation microelectronic and optoelectronic devices since they can function as both building units and interconnections.

Different synthesis methods have been used to prepare nanostructured MnO_2, including sol–gel [9], electrode deposition [10], reflux [11], coprecipitation [12], solid state chemical reaction [13], template-assisted treatment [14], and hydrothermal treatment [15]. Hydrothermal method is one of the most extensively used processes to prepare nanostructured MnO_2 with controlled morphologies and good properties. Generally, MnO_2 is synthesized by the oxidation of Mn(II) salts or the reduction of Mn(VII) salts. Many oxidants and reductants have been chosen to control the microstructures and morphologies during the above processes. Research shows that the molar ratio of oxidants and reductants, acidity, and temperature are important factors for the fabrication of MnO_2. For example, Umek et al. [16] synthesized 3D hierarchical α-MnO_2 nanotubes using concentrated H_2SO_4. By adjusting the volume of 1.0 M HCl solution, Zhou et al. [17] synthesized hollow urchins, columnar nanorod clusters, tetragonal nanotube clusters, and tetragonal nanorod clusters of α-MnO_2. Song et al. [18] reported the synthesis of α-MnO_2 urchins consisting of 180 nm wide nanorods using sodium dodecyl

Y. Zhang · Z. Zhu (✉)
School of Material Engineering, South West Petroleum University, Chengdu 610500, China
e-mail: zhu.zehua@163.com

Y. Zhang · H. Liu (✉) · K.-W. Wong · R. Mi · J. Mei · W.-M. Lau
Chengdu Green Energy and Green Manufacturing Technology R&D Center, Chengdu Development Center of Science and Technology, China Academy of Engineering Physics, Chengdu 610207, China
e-mail: mliuhao@gmail.com

sulfate as surfactant. DeGuzman et al. [19] obtained α-MnO_2 using $KMnO_4$ to $MnSO_4{\cdot}H_2O$ with a molar ratio of 0.72 when the pH was 1.7 or lower at a temperature ranging from 100 to 120 °C, and β-MnO_2 was formed when the temperature was higher than 120 °C. However, in most previous reports, size and morphology manipulation was achieved either under highly acidic conditions [16, 17] or through the use of surfactants [20]. Development of an acid-free hydrothermal route with a simultaneous control of phase and morphology of MnO_2 nanostructures is still desirable due to both environmental requirement and future application consideration.

To achieve this aim, we used a simple low-temperature hydrothermal method without adjusting the pH of the system to investigate the effect of synthesis temperature on the formation of MnO_2 crystalline structure. The method is straightforward and the MnO_2 crystalline structure can be simply controlled by reaction temperature. The electrochemical properties of the resultant MnO_2 nanowires with variable crystalline structure but similar morphology (which influence the nanowires' physical and chemical performance) were compared and investigated by the cyclic performance, cyclic voltammetry (CV) curves, and electrochemical impedance spectroscopy (EIS), respectively. Although our results show that structure variation of MnO_2 did not cause great differences in their lithium storage performance, our nanowires provide ideal experimental subjects to study the crystalline effect on many physical and chemical properties of MnO_2 since the morphology impact could be excluded.

2 Experimental section

2.1 Materials synthesis

The synthesis of α- and β-MnO_2 nanowires was carried out through a hydrothermal technique. In a typical synthesis process, 0.169 g of $MnSO_4{\cdot}H_2O$ and 0.158 g $KMnO_4$ were mixed in 10 ml deionized water to form a uniform precursor solution. After being stirred continuously for 10 min, the solution was transferred into a Teflon-lined stainless-steel autoclave (capacity: 23 ml), and then sealed and heated at given temperatures between 150 and 180 °C for 15 h. And then the autoclave was cooled to room temperature. The product was filtered, washed with distilled water, and then dried at 60 °C overnight in air.

2.2 Characterization

The obtained samples were characterized by X-ray diffraction patterns (XRD, Rigaku D/max 2500 diffractometer with Cu KR radiation), scanning electron microscopy (SEM, S-5200), and transmission electron microscope (TEM, Philips Tecnai F20 operating at 200 kV).

2.3 Electrochemical tests

The electrochemical measurements were carried out using CR 2032 coin cells with lithium metal as the counter and reference electrodes. The working electrodes were prepared by mixing 85 wt % active material with 5 wt % conductive carbon black and 10 wt % polyvinylidene fluoride (PVDF) dissolved in *N*-methyl-pyrrolidone (NMP). The slurry was then coated onto a copper foil and dried in a vacuum oven at 100 °C overnight. The electrolyte was the solution of 1 M $LiPF_6$ in a mixture of ethylene carbonate (EC) and dimethyl carbonate (DMC) with the volume ratio of 1:1, and Celgard 2400 membrane was used as the separator. The cells were assembled in an argon-filled glove box with oxygen and moisture content less than 0.1 ppm. Galvanostatical discharge–charge experiments were performed at a constant current density of 0.1 C in the voltage range between 3.00 and 0.01 V by the ARBIN measurement system at room temperature. Cyclic voltammetry (CV) test was carried out on CHI660D electrochemical workstation at a scanning rate of 0.5 mV s^{-1}. Alternating current (AC) impedance was recorded by applying a sine wave with an amplitude of 5.0 mV over the frequency range from 100 kHz to 100 mHz. The code Zview was used to fit the impedance spectra to the proposed equivalent circuit.

3 Results and discussion

X-ray diffraction patterns of MnO_2 nanowires synthesized at different temperature ranging from 150 to 180 °C are shown in Fig. 1 demonstrating the temperature effect on products structure. The diffraction peaks of the sample synthesized at 150 °C was indexed to α-MnO_2 (ICDD-JCPDS No. 44-0141) with lattice constants of $a = 0.9784$ and $c = 0.2863$ nm, while the product synthesized at 180 °C corresponds to the tetragonal phase β-MnO_2 (JCPDS No. 65-2821) with lattice constants of $a = 0.4399$ and $c = 0.2874$ nm. No impurity peaks are observed, indicating that high-purity α-MnO_2 and β-MnO_2 can be attained by simply changing the hydrothermal reaction temperature. The samples that synthesized between these two temperatures consist of both these two kinds of structures.

[MnO_6] octahedron is the basic structural unit for both α- and β-MnO_2, but interlinked in different ways by sharing corners or edges. The crystalline structures of α-MnO_2 are constructed from the double chains of edge-sharing [MnO_6] octahedra which are linked at the corners to form $(2 \times 2) + (1 \times 1)$ tunnel structures. β-MnO_2

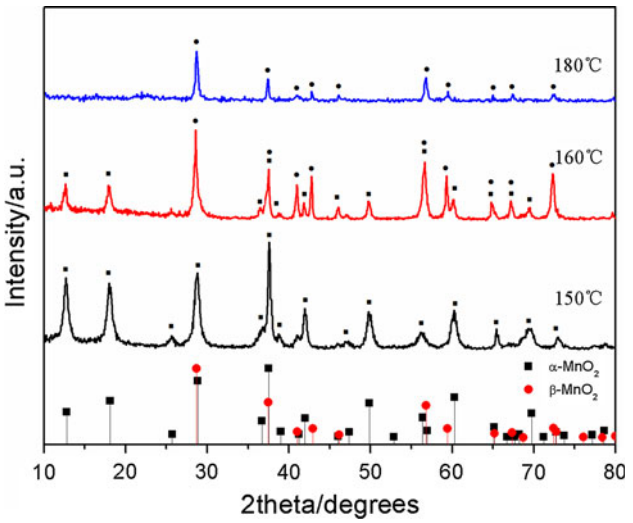

Fig. 1 X-ray diffraction patterns of different reaction temperature of prepared MnO_2. Symbols represent filled square α-MnO_2 (JCPDS 44-0141), filled circle β-MnO_2 (JCPDS 65-2821)

consists only of (1 × 1) tunnels separated by single chains [21]. After a high temperature reaction, pure β-MnO_2 was prepared (Fig. 1, 180 °C) because low crystalline α-MnO_2 transformed into β-MnO_2, which has a higher thermal stability. The (2 × 2) tunnel structure ramsdellite could be transformed into β-MnO_2 when the reaction temperature was higher than 150 °C [22], and β-MnO_2 could come from α-MnO_2 with a low degree of crystallinity without adjusting the pH of the system. It is believed that the difference in crystalline structure of MnO_2 phases would affect their electrochemical properties.

Further information of microstructure of the α-MnO_2 and β-MnO_2 was observed by SEM and TEM. Figure 2 shows the representative SEM and TEM images of the as-prepared MnO_2 samples at 150 and 180 °C separately. α-MnO_2 nanowires obtained at 150 °C have a uniform diameters distribution in the range of 40–70 nm and a length between 5 and 10 μm. In comparison, the diameter of β-MnO_2 synthesized at 180 °C ranges from 40 to 80 nm, and the length of β-MnO_2 nanowires is also around 5–10 μm. HRTEM analysis (Fig. 2c and d) shows a lattice spacing of 0.69 nm, which agrees well with (110) interplanar distance of α-MnO_2. The marked lattice fringes with a spacing of 0.28 nm are ascribed to the interplanar spacings (001) planes of β-MnO_2, respectively. The physical and chemical properties of MnO_2 nanowires have been found to be highly dependent on their chemical composition, crystallographic structure, as well as particle size and shape [23–25]. Our synthesized α- and β-MnO_2 nanowires, with similar diameter and length, provide very good candidates to study the effect of crystallographic structure on battery performance since the influence of shape and size has been minimized.

To characterize the electrochemical performance of different crystalline structured manganese dioxides electrode, the cyclic voltammograms (CVs) and first two discharge–charge (D–C) profiles of both α- and β-MnO_2 were carried out. Figure 3a and b shows the CV of prepared α- and β-MnO_2 in lithium ion half battery at a scanning rate of 0.1 mv s^{-1}. Clearly, the first scan cycle is slightly different from the subsequent ones. The curves clearly demonstrated that the redox peaks are corresponding to the absorption/desorption of lithium ions at the electrode surface and Li^+ insertion/extraction process in the lattice framework of MnO2, which agrees well with previous reports [26, 27]. The voltage plateaus for the first two D–C profiles shown in Fig 3c and d are consistent with redox peaks of CV curves.

In Fig. 3a and b, the main cathodic peaks shown in the first cycle are found at 1.5 and 0.2 V, corresponding to the decomposition of electrolyte and electrochemical reduction reaction of MnO_2 with Li, respectively. The observed main anodic peaks at 1.3 and 2.4 V are ascribed to the oxidation reaction. In comparison with the CV curves, the first two D–C profiles of α- and β-MnO_2 electrodes at a rate of 0.1 C are shown in Fig. 3c and d. The initial discharge capacities of α- and β-MnO_2 are 1365 mAh g^{-1} and 1060 mAh g^{-1}, respectively. The α-MnO_2 shows lower initial coulombic efficiency (36.5 %) than β-MnO_2 (49.6 %). The initial capacity loss may result from the incomplete conversion reaction and irreversible lithium loss due to the formation of a solid electrolyte interphase (SEI) layer [28].

The cycling performances of α-MnO_2 and β-MnO_2 in the voltage range of 0.01–3.0 V are displayed in Fig 4. The specific capacity for MnO_2 electrode decreased prominently with increasing cycle numbers. The α-MnO_2 displayed a discharge capacity of 125 mAh g^{-1} up to 60 cycles, whereas that of β-MnO_2 decreased to below 100 mAh g^{-1}. The capacity reduction of MnO_2 is likely due to the crystalline structure. For α-MnO_2, the two-tunnel structure is not stable and the incorporated K^+ ions may block the transportation of Li ions [28], resulting in low capacity and poor cyclicality. On the other hand, although the β-MnO_2 has a 1D structure containing (1 × 1) tunnels, the structure is not desirable for cation accommodation. Moreover, the loss of electrical contact between the particles caused by the large volume change during Li ion insertion/extraction also contributes to the capacity fading. Therefore, due to the difference in the crystalline structure of the MnO_2, Li ion diffusion/transportation trajectory is not the same, resulting in different capacities.

Electrochemical impedance spectroscopy, one of the principal methods to exam the fundamental behavior of electrode materials for LIBs, was employed to further understand the electrochemical performance of MnO_2. The impedance spectra from EIS of α-MnO_2 and β-MnO_2 were

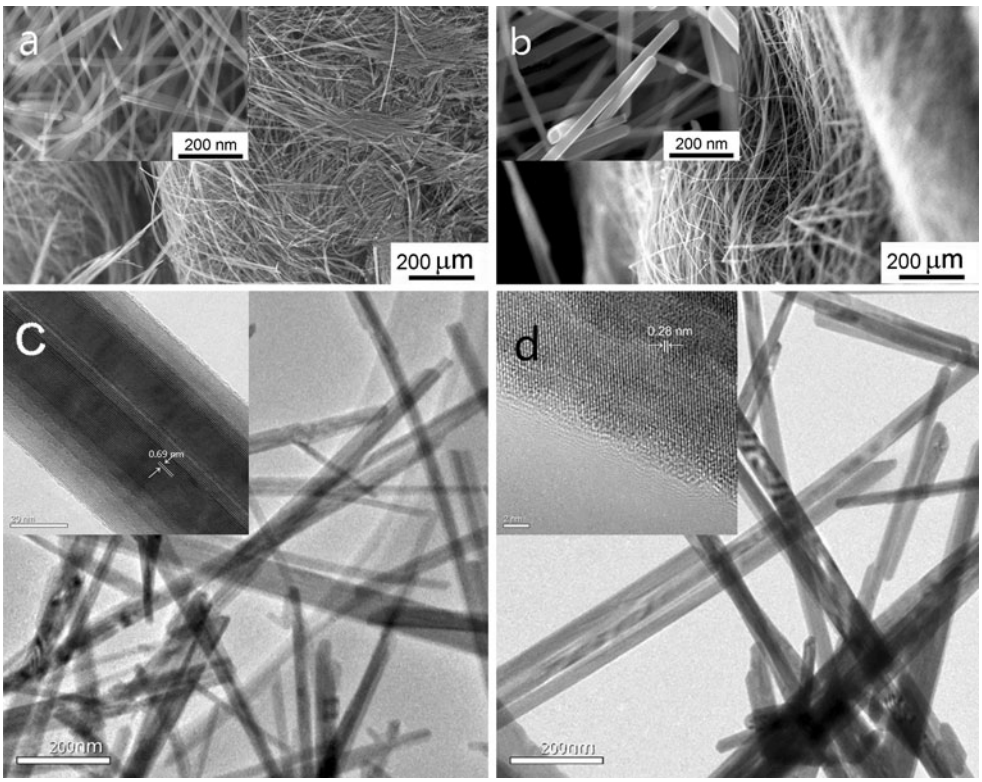

Fig. 2 SEM and TEM images of synthesized α-MnO_2 (**a**, **c**) and β-MnO_2 (**b**, **d**)

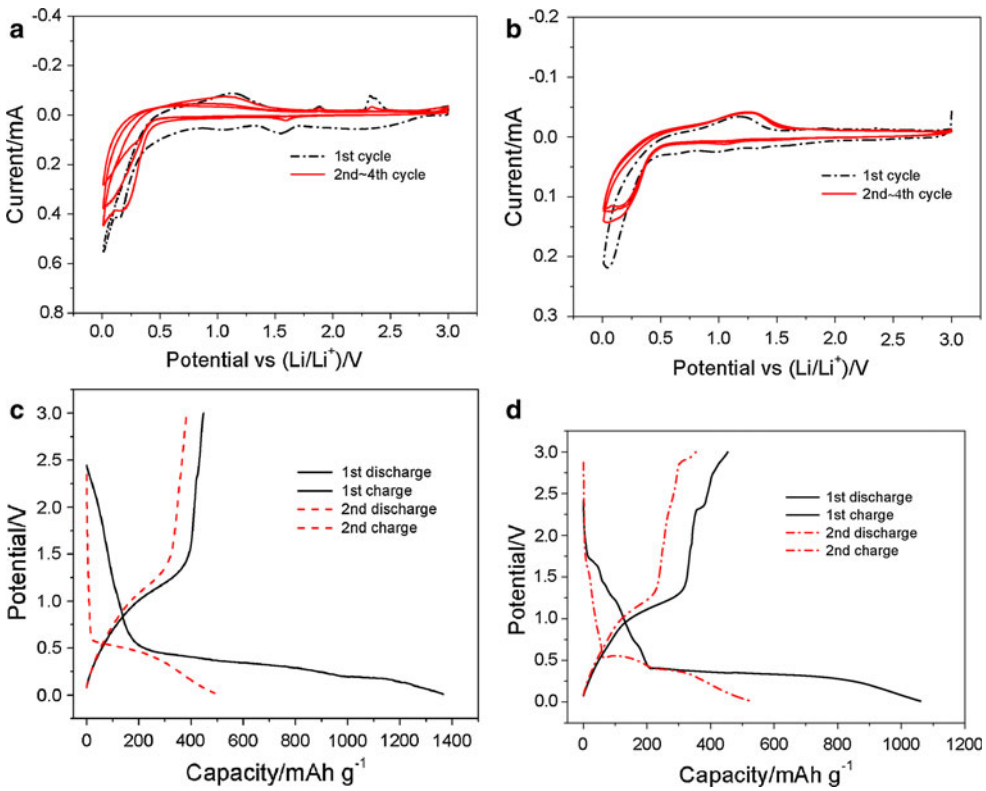

Fig. 3 First two discharge–charge curves of **a** α-MnO_2 and **b** β-MnO_2 between 0.01 and 3 V (vs. Li/Li^+). Cyclic voltammetry curves of **c** α-MnO_2 and **d** GMC electrode at a scan rate of 0.1 mV s^{-1}

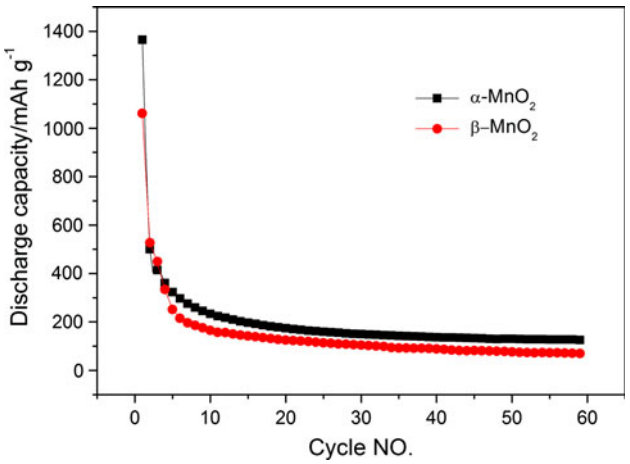

Fig. 4 Cycling performance of α-MnO_2 and β-MnO_2 electrode at 0.1 C rate

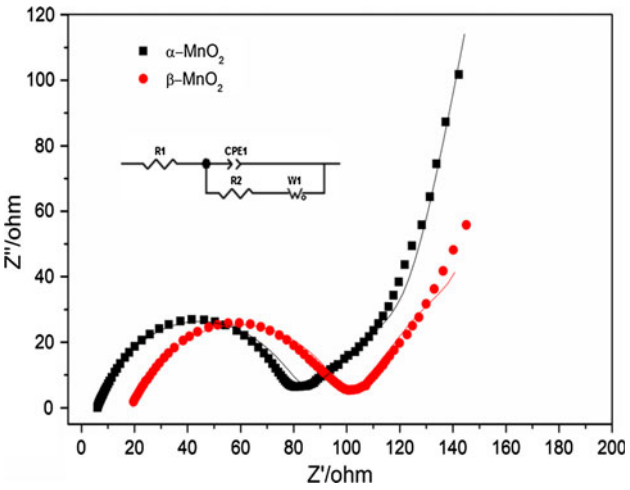

Fig. 5 Electrochemical impedance spectroscopy results of the α-MnO_2 and β-MnO_2

analyzed and fitted to the equivalent circuit as shown in Fig. 5. An impedance spectrum is usually a composite curve consisting of an arc at higher frequency region and a spike at lower frequency region [29]. In the equivalent circuit, $R1$ is the total resistance of electrolyte, electrode, and separator. $R2$ and *CPE1* correspond to the charge transfer resistance and the double-layer capacitance on the grain surface, respectively. W1 is known as the Warburg resistance and related to the frequency dependence of ion diffusion/transportation from the electrolyte to the electrode surface. It is shown that α-MnO_2 electrode has a much lower electrolyte resistance and charge transfer resistance ($R1 = 6.08$, $R2 = 74.58$) than those of β-MnO_2 ($R1 = 19.66$, $R2 = 80.84$). It confirms that different crystalline structure of MnO_2 could result in different conductivity and electron transport during the electrochemical lithium insertion/extraction.

4 Conclusions

In this present work, we used the facile hydrothermal approach to synthesized two types of MnO_2 nanostructure with similar morphology. By adjusting the reaction conditions, we proved that MnO_2 with the same size and shape but different crystalline structure had distinctive electrochemical activity. We also confirmed that although both α-MnO_2 and β-MnO_2 had large specific capacity initially, the poor cycle performance had proved that MnO_2 could not be used as electrode materials alone in lithium ion battery.

Acknowledgments The authors appreciate the support of the Science and Technology Foundation of China Academy of Engineering Physics (No.2012B0302041) and Graduate student innovation fund of the South West Petroleum University (No.GIFSS0714). We are indebted to Magaret Yau, Jiahui Lin, Jicheng Zhang, Jiangping Wang and Shaomin Li for their kind help and fruitful discussions.

References

1. Ching S, Driscoll PF, Kieltyka KS, Marvel MR, Suib SL (2001) Chem Commun 23:2486
2. Ryu WH, Han DW, Kim WK, Kwon HS (2011) J Nanopart Res 13:4777
3. Cheng F, Zhao J, Song W, Li C, Ma H, Chen J, Shen P (2006) Inorg Chem 45:2038
4. Jiang H, Zhao T, Ma J, Yan C, Li C (2011) Commun 47:1264
5. Zhang H, Cao G, Wang Z, Yang Y, Shi Z, Gu Z (2011) Nano Lett 8:2664
6. Kim MG, Cho J (2009) Adv Funct Mater 19:1497
7. Gao T, Glerup M, Krumeich F, Nesper R, Fjellvåg H, Norby P (2008) J Phys Chem C 112:1313
8. Yaqoob K, Shahid KD, Mazhar M, Muhammad RK (2011) J Mater Res 26:2268
9. Yang LX, Zhu YJ, Wang WW, Tong H, Ruan ML (2006) J Phys Chem B 110:6609
10. Chou S, Cheng F, Chen J (2006) J Power Sources 162:727
11. Xie J, Li X, Yu ZH, Zhang LJ, Li F, Xia DG (2010) Rare Met 29:187
12. Yan DW, Wang CR J Nanosci (2007) Nanotechnol 7:2487
13. Sugantha M, Ramakrishnan PA, Hermann AM, Warmsingh CP, Ginley DS (2003) Int J Hydrogen Energy 28:597
14. Xu NC, Liu ZH, Ma XR, Qiao SF, Yuan JQ (2009) J Nanopart Res 11:1107
15. Xiao W, Xia H, Fuh JYH, Lu L (2009) J Power Sources 193:935
16. Umek P, Gloter A, Pregelj M, Dominko R, Jagodic M, Jaglicic Z, Zimina A, Brzhezinskaya M, Potocnik A, Filipic C, Levstik A, Arcon D (2009) J Phys Chem C 113:14798
17. Zhou M, Zhang X, Wei J, Zhao S, Wang L, Feng B (2010) J Phys Chem C 115:1398
18. Song XC, Zhao Y, Zheng YF (2007) Cryst Growth Des 7:159
19. DeGuzman RN, Shen YF, Neth EJ, Suib SL, O'Young CL, Levine S, Newsam JM (1994) Chem Mater 6:815
20. Wang X, Li YD (2002) J Am Chem Soc 124:2880
21. Liu Z, Xing Y, Chen CH, Zhao LL, Suib SL (2008) Chem Mater 20:2069
22. Shen XF, Ding YS, Hanson JC, Aindow M, Suib SL (2006) J Am Chem Soc 128:4570
23. Seo WS, Jo HH, Lee K, Kim B, Oh SJ, Park JT (2004) Angew Chem Int Ed 43:1115

24. Cheng FY, Chen J, Gou XL, Shen PW (2005) Adv Mater 17:2753
25. Devaraj S, Munichandraiah N (2008) J Phys Chem C 112:4406
26. Jiao F, Bruce PG (2007) Adv Mater 19:657
27. Zhong KF, Xia X, Zhang B, Li H, Wang ZX, Chen LQ (2010) J Power Sources 195:3300
28. Chen WM, Qie L, Shao QG, Yuan LX, Zhang WX, Huang YH (2012) Appl Mater Interfaces 4:3047
29. Yan J, Fan ZJ, Wei T, Qian WZ, Zhang ML, Wei F (2010) Carbon 48:3825